Optics Letters

Post-ensemble generation with Airy beams for spatial and spectral switching in incoherent imaging

SHIVASUBRAMANIAN GOPINATH[1] AND VIJAYAKUMAR ANAND[1,2,*]

[1]Institute of Physics, University of Tartu, W. Ostwaldi 1, 50411 Tartu, Estonia
[2]Optical Sciences Center, Swinburne University of Technology, Melbourne, Victoria 3122, Australia
*vijayakumar.anand@ut.ee

Received 26 February 2024; revised 15 May 2024; accepted 16 May 2024; posted 22 May 2024; published 31 May 2024

Spatial, temporal, and spectral resolutions and field-of-view are important characteristics of any imaging system. In most, if not all, it is impossible to change the above characteristics after recording a digital picture, video, or hologram. In recent years, there have been investigations on the possibilities to change the above characteristics post-recording. In this Letter, for the first time, to the best of our knowledge, we report novel recording and reconstruction methods built upon the principles of coded aperture imaging that allow changing the axial and spectral resolutions post-recording. We named this method—post-ensemble generation with Airy beams for spatial and spectral switching (PEGASASS). In PEGASASS, light from an object point is converted into Airy beams and recorded such that every recording has a unique Airy pattern. An ensemble of Airy patterns is constructed post-recording and the axial and spectral resolutions are tuned by controlling the chaos in the ensemble. The above tunability is achieved without adversely affecting the lateral resolution. Proof-of-concept experimental results of PEGASASS in 3D in both (x,y,z) and (x,y,λ) and 4D in (x,y,z,λ) are presented. We believe that PEGASASS has the potential to revolutionize the field of imaging and holography.

https://doi.org/10.1364/OL.522319

Lateral resolution (LR), axial resolution (AR), temporal resolution (TR), spectral resolution (SR), and field-of-view (FoV) are key characteristics of an imaging system. The LR and AR measure the imaging system's capability to discriminate features of an object along the transverse and longitudinal directions in space. The TR measures the system's capability to discriminate events in time. The SR measures the system's ability to discriminate information based on a wavelength. The LR and AR are dependent upon the numerical aperture (NA) of the imaging system given as $\sim\lambda/\mathrm{NA}$ and $\sim\lambda/\mathrm{NA}^2$ respectively [1], where NA is $\sim D/2f$, f is the focal length, and D is the diameter of the entrance pupil or the lens. The LR and AR of an imaging system are fixed once the imaging system is built with a one-to-one relation between the LR and AR. The SR in a regular imaging system is set by the color filters in the image sensor [2]. The TR in a regular imaging system depends upon the frame rate of an image sensor [3]. The FoV is limited by the size of the image sensor and is inversely related to LR [4]. The above interdependencies exist in all conventional lens-based imaging systems. The interdependencies often create limitations in an imaging task, and it is desirable to relax at least some of the above interdependencies for certain applications. For instance, when recording a sparse 3D sample, it is desirable to decrease the AR without affecting the LR such that multiple planes of the sample can be imaged simultaneously resulting in a rapid investigation. However, according to the constructs of conventional imaging systems, the AR can be decreased only by decreasing the LR. Similarly, it is desirable to increase the FoV without adversely affecting the LR and record events faster than the refresh rate of the image sensor.

In recent years, coded aperture imaging (CAI) techniques have offered new realities with flexible computational optical frameworks to image beyond the limitations of conventional imaging systems. Lensless imaging systems have been developed to relax the FoV and LR interdependency [5]. Imaging modalities have been proposed and demonstrated to record fast transient events beyond the limits of the image sensor [6]. CAI techniques to obtain color images with a monochrome image sensor were developed [7–9]. Extending the FoV beyond the limit imposed by the image sensor was reported [10,11]. Several studies on CAI to tune AR independent of LR were reported [12].

The main advantage of incoherent digital holography and certain CAI techniques over conventional incoherent imaging is digital refocusing, i.e., the capability to reconstruct different planes of a multiplane object after recording. The above capability does not exist in conventional incoherent imaging methods, where mechanical refocusing involving either shifting the location of the object, lens, or sensor is required. While tuning the AR independent of LR was demonstrated in some recent research [12], it is impossible to tune the AR after recording a scene as a digital picture or a hologram. In 2023, an incoherent hybrid imaging system based on CAI was demonstrated in which the possibility to tune the AR without affecting the LR after recording a digital picture for the first time [13]. Certain CAI approaches also have the capability to tune AR post-recording [14]. In this study, we propose a novel CAI method—post-ensemble generation with Airy beams for spatial and spectral switching (PEGASASS) for tuning not only AR but also SR without affecting the LR after recording a digital picture or a video. Considering the significant impact, the above-mentioned post-digital refocusing in digital holography had over real-time

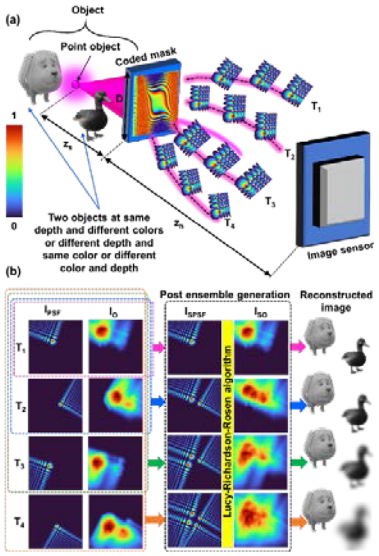

Fig. 1. (a) Optical configuration of PEGASASS and (b) its imaging process.

mechanical refocusing in regular imaging, a similar impact can be expected from the post-digital tuning of AR and SR over physical real-time changes in optical components. This method can be implemented using other beams such as a Bessel beam that has long axial and spectral correlation lengths. However, with Airy beams, asymmetric intensity distributions and unique 3D paths can be achieved allowing the creation of sophisticated ensembles.

The optical configuration of PEGASASS is shown in Fig. 1. Light from an object point with an amplitude of $\sqrt{I_s}$ reaches a coded mask located at a distance of z_s with a complex amplitude of $\sqrt{I_s}C_1 L\left(\frac{\bar{r}_s}{z_s}\right) Q\left(\frac{1}{z_s}\right)$, where C_1 is a complex constant, $Q(a) = \exp[i\pi a\lambda^{-1}(x^2+y^2)]$ and $L\left(\frac{\bar{s}}{z}\right) = \exp[i2\pi(\lambda z)^{-1}(s_x x + s_y y)]$ are the quadratic and linear phase functions, respectively. The coded mask in PEGASASS is a cubic phase mask (CPM) given as $\exp[j\Phi_{CPM}(k)] = \exp\left[-j\frac{2\pi}{\lambda}\{\xi_k(x_k+\Delta x_k)^3 + \eta_k(y_k+\Delta y_k)^3\}\right]$. The variables $x_k = x_0 cos\theta_k + y_0 sin\theta_k$ and $y_k = y_0 cos\theta_k - x_0 sin\theta_k$ can be used to rotate the coordinate system, and k is an integer varying from 1 to M corresponding to times $T_{k=1}$ to $T_{k=M}$, and M is the number of camera recordings. The shift parameters Δx_k and Δy_k can be used to shift the origin of the CPM, and the scaling factors ξ_k and η_k can change the magnifications along the x and y directions, respectively. The complex amplitude after the CPM is given as $\sqrt{I_s}C_1 L\left(\frac{\bar{r}_s}{z_s}\right) Q\left(\frac{1}{z_s}\right) \exp[j\Phi_{CPM}(k)]$. The intensity distribution recorded at a distance of z_h from the CPM is given as $I_{PSF}(\bar{r}_0;\bar{r}_s,z_s,k) = \left|\sqrt{I_s}C_1 L\left(\frac{\bar{r}_s}{z_s}\right) Q\left(\frac{1}{z_s}\right) \exp[j\Phi_{CPM}(k)] \otimes Q\left(\frac{1}{z_h}\right)\right|^2$, where '⊗' is a 2D convolutional operator. The above expression can be simplified into $I_{PSF}(k) = \left|Ai_k\left(\frac{x_k}{a_k},\frac{y_k}{a_k}\right)\right|^2$ where Ai is the truncated Airy function, and a_k is the scaling factor of the Airy function. Like most CAI systems, PEGASASS is also a linear shift-invariant system and therefore, the point spread function can be expressed as $I_{PSF}(\bar{r}_0;\bar{r}_s,z_s,k) = I_{PSF}\left(\bar{r}_0 - \frac{z_h}{z_s}\bar{r}_s;0,z_s,k\right)$, where z_h/z_s is the magnification. The object intensity distribution for a 2D object consisting of N points given as $o(\bar{r}_s) = \sum_p^N b_p\delta(\bar{r}-\bar{r}_{s,p})$ is given as $I_O(\bar{r}_0;z_s,k) = \sum_p^N b_p I_{PSF}\left(\bar{r}_0 - \frac{z_h}{z_s}\bar{r}_{s,p};0,z_s,k\right)$.

In PEGASASS, synthetic point spread functions and object intensity distributions are created by constructing identical ensembles post-recording given as $I_{SPSF}(\lambda,z) = \sum_{k=1}^M \gamma_k I_{PSF}(\lambda,z,k)$ and $I_{SO} = \sum_{k=1}^M \gamma_k I_O(k)$, where γ_k is the weight of the k^{th} intensity distribution. The image of the object corresponding to a particular pair (λ,z) can be reconstructed by processing I_{SO} with $I_{SPSF}(\lambda,z)$ using one of the many deconvolution methods [15]. The information corresponding to $\lambda' \neq \lambda$ and $z' \neq z$ appears blurred and forms the background. In regular CAI methods, the degree of blur is directly proportional to $\Delta\lambda$ and Δz. This cannot be changed after the recording. But in PEGASASS, this degree of blur is tunable post-recording by changing M. When M is increased, the blur increases and vice versa.

A recently developed deconvolution method Lucy–Richardson–Rosen algorithm (LRRA) has been used in this study. The g^{th} reconstructed image from LRRA is given as $I_R(g) = I_R(g-1)\left[\frac{I_{SO}}{I_R(g-1)\otimes I_{SPSF}} *_\beta^\alpha I_{SPSF}\right]$, where '$*_\beta^\alpha$' is the non-linear correlation operator given as $u *_\beta^\alpha v = \mathcal{F}^{-1}\{|U|^\alpha |V|^\beta \exp(i\Phi_U)\cdot\exp(-i\Phi_V)\}$, where U and V are the spectra of u and v respectively. The above imaging process is based on the properties of spatially incoherent light and applicable to most CAI imaging systems that use a spatially incoherent illumination. When $M=1$, there is only a single Airy pattern with a low AR and SR, and the imaging of a thick object will reconstruct all the planes of the object within the long focal depth due to the non-diffractive nature of the Airy beam. However, when M is increased, even though the individual Airy beams still retain their respective non-diffractive natures, cumulatively the non-diffractive nature weans off. This is because the Airy patterns are unique and have relative changes in the location with respect to one another resulting in lower correlation values for non-matching depths and wavelengths causing an increase in blur of information from non-matched wavelengths and depths. This effect results in an increase in AR and SR. However, for all values of M, the LR remains a constant as the above do not affect the lateral correlation length. It is possible to tune the AR and SR continuously by varying M as well as γ, i.e., the AR and SR values between the limits of $M=1$ and $M=2$ is achieved by tuning γ between 0 and 1 continuously. In real-time tuning of AR as discussed in [12], it is impossible to achieve continuous tunability of AR as many values of AR require a high contrast in intensity between Airy patterns.

The imaging process of PEGASASS is based on the principles of spatially incoherent illumination for the recording part and spatially as well as temporally incoherent illumination for the computational processing part. Considering CAI with either coherent or spatially incoherent illumination, for a point object, there is only self-interference between different beams generated by the coded mask. When there is more than one point, in the same system, there is mutual interference in addition to self-interference in the case of coherent illumination. With spatially incoherent illumination, there is self-interference between beams generated from a single point and intensity addition between beams generated from different points. In PEGASASS, for a single point, instead of self-interference, there is only an

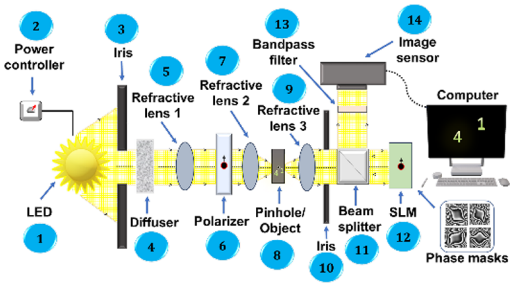

Fig. 2. Schematic of the experimental setup.

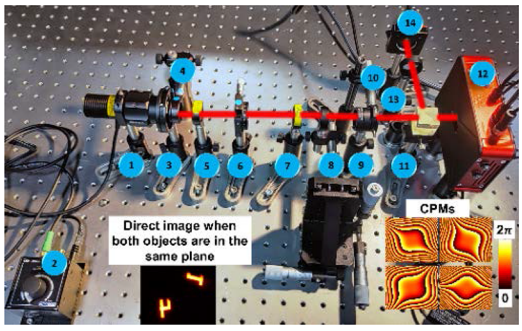

Fig. 3. Photograph of the experimental setup. The four CPMs displayed on the SLM are shown at the bottom. Direct image of the objects at $z_s = 5$ cm is shown as an inset.

intensity addition which makes the system unique. In CAI, for both coherent and spatially incoherent illuminations, for a single point, when there are two Airy beams ψ_1 and ψ_2 generated by the coded mask, at the sensor plane, the intensity distribution is $I = |\psi_1 + \psi_2|^2$ in the region of interaction. For PEGASASS, the case is different with only an intensity addition given as $I = \gamma_1|\psi_1|^2 + \gamma_2|\psi_2|^2$.

The schematic and photograph of the experimental setup are shown in Figs. 2 and 3 respectively with different elements (E) labeled by numbers. Two light sources high-power red LED ($\lambda = 660$ nm, 940 mW, and $\Delta\lambda = 20$ nm) and a high-power green LED (Thorlabs, $\lambda = 554$ nm, 650 mW) were used for this study. In the first part of the experiment, the red LED (E1) with a power controller (E2) is used for illumination. An iris (E3), diffuser (Thorlabs Ø1" Ground Glass Diffuser-220 GRIT) (E4), and a refractive lens with f = 5 cm (E5) were used to remove the image of the grating lines of the LED from the beam. The collimated light from E5 enters the polarizer (E6), which is oriented along the active axis of the spatial light modulator (SLM) (Thorlabs Exulus HD2, 1920×1200 pixels, pixel size = 8 μm) (E12). A refractive lens 2 with f = 5 cm (E7) is used to critically illuminate the pinhole/object (E8). The light from the pinhole/object is collimated by a refractive lens with f = 5 cm (E9), and its diameter is controlled by an iris (E10). The collimated light enters the beam splitter (E11) and reaches the SLM. The CPMs for the generation of Airy beams shown in bottom of Fig. 3 were displayed on the SLM one after the other, and the corresponding holograms were recorded by the image sensor (Zelux CS165MU/M 1.6 MP monochrome CMOS camera, 1440×1080 pixels with pixel size ~3.5 μm) (E14) which is located at a distance of $z_h = 17.8$ cm from the SLM. A bandpass filter (Thorlabs FLH633-5, $\lambda = 633$ nm and $\Delta\lambda = 5$ nm) (E13) was used to improve the visibility of the recorded holograms.

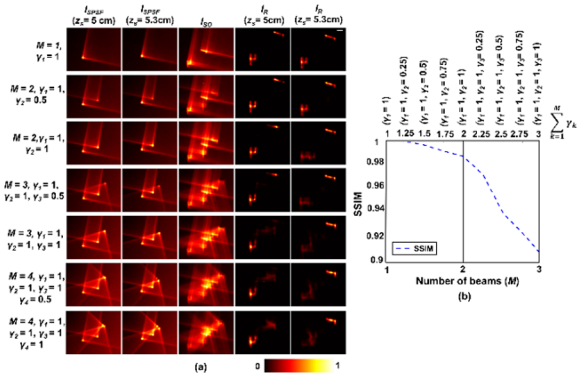

Fig. 4. (a) Column 1: I_{SPSF} ($z_s = 5$ cm), column 2: I_{SPSF} ($z_s = 5.3$ cm), column 3: I_{SO}, column 4: reconstruction results for I_R ($z_s = 5$ cm), and column 5: reconstruction results for I_R ($z_s = 5.3$ cm), for $M = 1$ to 4 and $\lambda = 633$ nm. (b) Plot of SSIM for different number of beams. Scale bar—100 μm.

A pinhole with a diameter of 50 μm was used for recording the I_{PSF}s, and two test objects digits '4' (object 1) and '1' (object 2), from Group-3 chosen from the R1DS1N-Negative 1951 USAF Test Target, Ø1" were used to record the I_O. The I_Os were recorded when object 1 and object 2 were mounted at depths $z_s = 5$ and 5.3 cm respectively. The I_{PSF}s were also recorded at those locations.

The experimental results of 3D imaging (x, y, z) with AR control post-recording are shown in Fig. 4(a). Columns 1 and 2 show the I_{SPSF} ($z_s = 5$ cm) and I_{SPSF} ($z_s = 5.3$ cm) for $M = 1$ to 4 and γ incremented by 0.5. Column 3 shows the I_{SO} where '4' and '1' are located at $z_s = 5$ cm and $z_s = 5.3$ cm, respectively. Columns 4 and 5 show the reconstruction results I_R ($z_s = 5$ cm) and I_R ($z_s = 5.3$ cm) by LRRA. When $M = 1$ and reconstruction using I_{SPSF} corresponds to the first object's location, both '4' and '1' were reconstructed perfectly even though they were at different depths, which indicates a low AR. When $M = 2$ and $\gamma_2 = 0.5$, again reconstructed using I_{SPSF} of $z_s = 5$ cm, object '4' is reconstructed but object '1' is blurred indicating an increase in AR. When the reconstruction is carried out using the I_{SPSF} of '1' then '4' appears slightly blurred indicating an increase in AR. When M is increased further, the object from the non-matching plane is more blurred showing an increase in AR. The changes in AR are seen by a change in blur which we have quantified using a figure of merit, namely, structural similarity index (SSIM). The SSIM values were calculated for the reconstructed images when $k > 1$ with respect to the reference when $k = 1$. The variation of SSIM indicating the variation of AR with respect to k is shown in Fig. 4(b). When the number of beams increased, the blur increased resulting in a decrease in SSIM, demonstrating an improvement in AR.

The experimental results of 3D imaging (x, y, λ) with SR control post-recording are shown in Fig. 5(a). The green LED with a bandpass filter (Thorlabs FLH532-4, $\lambda = 532$ nm and $\Delta\lambda = 4$ nm) was used for experiments with a different wavelength. In this experiment, the depth was maintained constant for both objects at $z_s = 5.3$ cm, but the wavelength was varied between the green illumination for '4' and red illumination for '1'. Column 1 shows the I_{SPSF} ($\lambda = 532$ nm), and column 2 shows the I_{SPSF} ($\lambda = 633$ nm). Column 3 shows the I_{SO}. Columns 4 and 5 show the reconstruction results corresponding to $\lambda = 532$ nm and $\lambda = 633$ nm, respectively, by LRRA. When $M = 1$, both objects

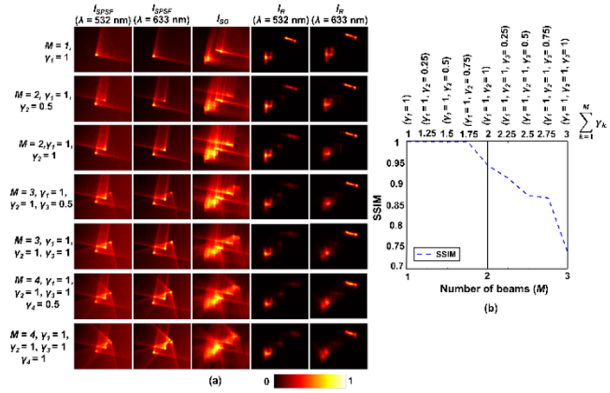

Fig. 5. (a) Column 1: I_{SPSF} ($\lambda = 532$ nm), column 2: I_{SPSF} ($\lambda = 633$ nm), column 3: I_{SO}, column 4: I_R ($\lambda = 532$ nm), and column 5: I_R ($\lambda = 633$ nm), for $M = 1$ to 4 and $z_s = 5.3$ cm for both objects. (b) Plot of SSIM for different number of beams.

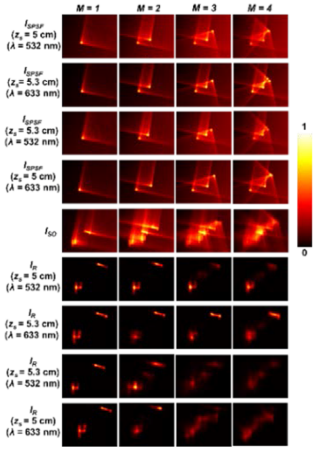

Fig. 6. Row 1 shows I_{SPSF} ($z_s = 5$ cm, $\lambda = 532$ nm), and row 2 shows I_{SPSF} ($z_s = 5.3$ cm, $\lambda = 633$ nm) for $M = 1$ to 4, and $\gamma = 1$. Rows 3 and 4 show the I_{SPSF} ($z_s = 5.3$ cm, $\lambda = 532$ nm) and I_{SPSF} ($z_s = 5$ cm, $\lambda = 633$ nm) for $M = 1$ to 4, and $\gamma = 1$. Row 5 shows the I_{SO} obtained from '4' at ($z_s = 5$ cm, $\lambda = 532$ nm) and '1' at ($z_s = 5.3$ cm, $\lambda = 633$ nm). Rows 6–9 show the reconstruction results of row 5 by reconstruction functions of rows 1 to 4, respectively, by LRRA.

are reconstructed perfectly for both colors when reconstructed with I_{SPSF} of green, which indicates a low SR. When $M = 2$, $\gamma_2 = 0.5$, the object corresponding to the color of the reconstruction function I_{SPSF} is reconstructed perfectly, but the object illuminated by a different color light appears blurred indicating a higher SR than that for $M = 1$. When M is increased further, the blurring effect also increases, demonstrating an improvement in SR. The variation of SSIM indicating the variation of SR with respect to k is shown in Fig. 5(b). Once again, when the number of beams increased, the blur increased resulting in a decrease in SSIM demonstrating an improvement in SR.

The experimental results of 4D imaging (x, y, z, λ) with simultaneous control of AR and SR post-recording are shown in Fig. 6. Row 1 shows I_{SPSF} ($z_s = 5$ cm, $\lambda = 532$ nm), and row 2 shows I_{SPSF} ($z_s = 5.3$ cm, $\lambda = 633$ nm) for $M = 1$ to 4, and $\gamma_k = 1$ for all k. Rows 3 and 4 show the I_{SPSF} ($z_s = 5.3$ cm, $\lambda = 532$ nm) and I_{SPSF} ($z_s = 5$ cm, $\lambda = 633$ nm) for $M = 1$ to 4, and $\gamma = 1$. Row 5 shows the I_{SO} obtained from '4' at ($z_s = 5$ cm, $\lambda = 532$ nm) and '1' at ($z_s = 5.3$ cm, $\lambda = 633$ nm). Rows 6 to 9 show the reconstruction results of row 5 by reconstruction functions of rows 1 to 4 respectively, by LRRA. From the results, similar effects of blurring can be noticed as seen in Figs. 4 and 5. However, it is possible to extract, depth-specific and wavelength-specific information from row 5. The strengths of the object information from other depths and wavelengths can be tuned post-recording by tuning M. The typical range of values of α, β, and the number of iterations were 0.2 to 0.4, 1, and 20 to 80 iterations respectively for this entire experimental study.

In conclusion, a novel CAI method PEGASASS has been developed for tuning AR and SR completely post-recording. The preliminary results are promising. One drawback with PEGASASS is the loss of TR due to multiple camera recordings. However, considering the 4D imaging capability with attractive AR and SR flexibilities post-recording and the fact that most inline incoherent digital holography techniques require three camera shots, the penalty is not high. With a color sensor, it is possible to tune the SR after recording by extracting and processing information channel-wise but impossible with monochrome sensors. With CAI moving toward color imaging without a color camera and virtual staining, no method is available as of today to tune the SR after recording. We believe that PEGASASS can be a powerful tool to achieve flexibility in the current state-of-the-art CAI techniques. It is also believed that this approach can open new pathways to achieve fully flexible imaging systems along all dimensions in the future.

Funding. HORIZON EUROPE Widening Participation and Strengthening the European Research Area (857627 (CIPHR)); Australian Research Council (DP240103231).

Acknowledgment. The authors thank Aravind Simon for the useful discussions.

Disclosures. The authors declare no conflicts of interest.

Data availability. Data underlying the results presented in this paper are not publicly available at this time but may be obtained from the authors upon reasonable request.

REFERENCES

1. H. H. Barrett and K. J. Myers, *Foundations of Image Science* (Wiley, 2004).
2. O. Flasseur, C. Fournier, N. Verrier, *et al.*, Appl. Opt. **56**, F189 (2017).
3. T. G. Etoh, A. Q. Nguyen, Y. Kamakura, *et al.*, Sensors **17**, 483 (2017).
4. U. Leischner, W. Zieglgänsberger, and H. U. Dodt, PLoS One **4**, e5785 (2009).
5. H. Wang, Z. Göröcs, W. Luo, *et al.*, Optica **3**, 1422 (2016).
6. J. Liang and L. V. Wang, Optica **5**, 1113 (2018).
7. A. Wagadarikar, R. John, R. Willett, *et al.*, Appl. Opt. **47**, B44 (2008).
8. S. K. Sahoo, D. Tang, and C. Dang, Optica **4**, 1209 (2017).
9. A. Vijayakumar and J. Rosen, Opt. Lett. **42**, 947 (2017).
10. T. Igarashi, M. Naruse, and R. Horisaki, Opt. Express **31**, 31369 (2023).
11. M. R. Rai, A. Vijayakumar, and J. Rosen, Opt. Lett. **43**, 1043 (2018).
12. J. Rosen and V. Anand, Photonics **11**, 115 (2024).
13. S. Gopinath, A. S. J. F. Rajeswary, and V. Anand, Opt. Lasers Eng. **172**, 107837 (2024).
14. M. R. Rai and J. Rosen, Opt. Express **29**, 1634 (2021).
15. J. Rosen and V. Anand, Opt. Express **32**, 1034 (2024).